Seismicity properties of the Chain Transform Fault inferred using data from the PI-LAB experiment

K. Leptokaropoulos[1], C. A. Rychert[1], N. Harmon[1] and J. M. Kendall[2]

[1]*Ocean and Earth Science, University of Southampton, Southampton, UK*

[2]*Department of Earth Sciences, University of Oxford, Oxford, UK*

Corresponding author: Konstantinos Leptokaropoulos (K.Leptokaropoulos@soton.ac.uk)

Abstract

Oceanic transform faults are intriguing in that they do not produce earthquakes as large as might be expected given their dimensions. We use 1-year of local seismicity recorded on an array of ocean bottom seismometers (OBS) and geophysical data to study the seismotectonic properties of the Chain transform, located in the equatorial Mid-Atlantic. We extend our analysis back in time by considering stronger earthquakes (M_W 5.0) from global catalogs. We divide Chain into three areas (eastern, central, and western) based on multi-dimensional OBS seismicity cluster analysis. Seismic activity recorded by the OBS is the highest at the eastern area of Chain where there is a lozenge shaped topographic high, a negative rMBA gravity anomaly, and only a few historical M_W 5.5 events. OBS seismicity rates are lower in the western and central areas. However, these areas accommodate the majority of seismic moment release, as inferred from both OBS and historical data. We find no evidence of remote dynamic triggering and only weak evidence of tidal and static stress triggering. Higher b-values are significantly correlated with lower rMBA and also with shallower bathymetry, potentially related to thickened crust. Our results suggest high lateral heterogeneity along Chain: Patches with moderate to low OBS seismicity rates that occasionally host M_W 6.0 earthquakes are interrupted by segments with abundant OBS activity but few historical events with 5.5 $M_W < 6.0$. This segmentation is possibly due to variable fluid circulation and alteration, which may also be variable in time.

Plain Language Summary

Oceanic transform faults typically host earthquakes much smaller than expected based on their total seismogenic area. We study the seismotectonic properties of the Chain transform fault by combining 1-year of seismicity recorded by an ocean bottom seismometer (OBS) array with geophysical data (bathymetry, tidal height, gravity anomalies). We supplement our analysis with strong historical earthquakes (M 5.0) from global catalogs. Our cluster analysis of the OBS seismicity divides Chain into three areas: The eastern area is characterized by the highest OBS seismicity rates, negative gravity anomalies, large topographic highs and few historical events with 5.5 $M < 6.0$. The western and central areas demonstrate lower OBS seismicity rates. However, they occasionally produce M 6.0, being responsible for most of the total seismic energy release. Higher numbers of stronger events occur in areas with negative gravity anomalies and shallower water depths. No triggering of OBS seismicity from distant

strong earthquakes was detected. We find weak indications that OBS seismicity is influenced by ocean tides and strong (M 5.0), local events. Our results suggest high lateral heterogeneity along Chain, with alternating seismic and aseismic patches, variable crustal thickness, different degrees of hydrothermal circulation/alteration and potentially time-dependent behavior.

1. Introduction

Oceanic transform faults (TF)s are steeply dipping segments of young oceanic lithosphere bounded between mid-ocean ridge spreading centers. They are thought to have a simple structure in comparison to their continental counterparts given that the composition of the ocean crust and upper mantle is relatively homogenous and generally lacks the complex lateral variability commonly evident in the continental crust (e.g., Wolfson-Schwehr & Boettcher, 2019; Behn et al., 2007). Along the axis of an oceanic TF, lithospheres of different age, and thus with different thermal and mechanical properties, interact. The subsurface within slow-slipping TFs and their fracture zone extensions is often characterized by a thin, highly fractured and altered crust, often with partially or entirely absent gabbroic layer (Gregg et al., 2007; Marjanovic et al., 2020 and references therein).

Ridge-transform plate boundaries may also enhance hydrothermal circulation, substantially impacting geophysical, geochemical and biological processes (e.g., Hensen et al., 2019). The inside corner of a ridge-transform intersection in slow spreading ridges, such as the Mid-Atlantic Ridge (MAR), often accommodates characteristic morphological structures known as oceanic core complexes (e.g., Cann et al., 1997). Core complexes may be linked to hydrothermal fluid flow (such as in the Lost City Hydrothermal Field, North Atlantic) and extended hydrothermal vent systems (Kelley et al., 2001). Fault-linked fluid pathways along with large thermal gradients allow serpentinization of the oceanic mantle (Escartín & Cannat, 1999; Früh-Green et al., 2016). Such phenomena are plausibly very typical in marine transform systems. This is evidenced by the exposure of altered peridotites and gabbro at detachment faults along fracture zones and core complexes (Blackman et al., 1998), indicating that mantle serpentinization, at different degrees, may be common at the MAR. Transform faults themselves may exhibit fault zone damage which can also contribute to hydrothermal circulation and alteration along the transform valley (Froment et al., 2014; Kohli et al., 2021).

Most of the seismicity within the MAR is concentrated along ridge spreading centers and TFs, with the latter typically hosting larger magnitude events (with M_W up to around 7.0) and having unusually high stress drops and apparent stress compared to the global average for TFs (Scholz, 2019). It has been, nevertheless, continuously acknowledged (e.g., Brune, 1968) that oceanic TFs accommodate much fewer and smaller events (i.e., less seismic moment release) than would be anticipated considering the global scaling relationships between fault dimensions and earthquake size (e.g., Wells & Coppersmith, 1994). This is because slip along TFs takes place by both seismic (earthquakes) and aseismic (creep-

ing) processes, with the majority of slip occurring either aseismically or released by microseismicity and earthquake swarms in the mantle (Boettcher & Jordan, 2004; Roland et al., 2010; Kuna et al., 2019). The estimated low seismic coupling at TFs has led to the idea that stresses in oceanic TFs are primarily driven by slow transients, with earthquakes (fast ruptures) being just "aftershocks" of the creeping or silent events (Boettcher & Jordan, 2004). Although there is a great variation of seismic coupling among marine TFs (Wolfson-Schwehr & Boettcher, 2019), the work of Boettcher & Jordan (2004) found that a global mean of ~15 % of transform lengths are coupled, after binning by thermal area and averaging, assuming the classical brittle-ductile transition at the 600 °C isotherm prediction from thermal models (Abercrombie & Ekstrom, 2001; Behn et al., 2007). This may be maximum estimate if the brittle-ductile transition occurs deeper. TF earthquakes have been located at deeper depths than these predictions (Schlaphorst et al., 2022; Kuna et al., 2019; McGuire et al., 2012; Marjanović et al., 2020). This could be owing to greater amounts of hydrothermal alteration (Schlaphorst et al., 2022; Marjanović et al., 2020) than accounted for in predictions (Roland et al., 2010). Alternatively, ruptures at higher temperatures might be expected at transforms owing to the relatively high strain rates (Molnar, 2020). Finally, exhumed mylonites were used to argue that brittle and ductile deformation can both occur anywhere between 300 °C – 1000 °C (Kohli et al., 2021).

Our current knowledge of the structure and dynamics of oceanic TFs is limited by their remote location, hundreds or thousands of kilometers away from the continents, where seismometers are typically installed. Most of the available seismicity data come from teleseismic events, found usually in catalogs with high magnitudes of completeness (M_C > ~5.0). Such studies, although important (e.g., Engeln et al., 1986), can only offer a limited insight into the seismotectonic processes of MAR and the adjacent TFs. Higher resolution constraints on seismicity in these remote areas can be facilitated by specifically targeted deployment of instruments, including networks of Ocean Bottom Seismometers (OBS).

Two such expeditions were carried out in March 2016 and March 2017 for deployment and recovery of geophysical instrumentation at the equatorial MAR. Chain TF as well as the adjacent spreading centers and fracture zones were comprehensively studied under the framework of the PI-LAB (Passive Imaging of the Lithosphere-Asthenosphere Boundary) and the EURO-LAB (Experiment to Unearth the Rheological Lithosphere-Asthenosphere Boundary) projects. In addition to deploying 39 OBSs and 39 ocean bottom magnetotelluric instruments, multibeam bathymetry and back scatter imagery, gravity and magnetic data were collected (Harmon et al., 2018). These data have been used in studying ocean waves, crust and mantle structures, tidal triggering at an adjacent ridge segment, and morphotectonic properties of the area (e.g., Agius et al., 2018; 2021; Bogiatzis et al., 2020; Harmon et al., 2020; 2021; Wang et al., 2020; Leptokaropoulos et al., 2021; Rychert et al., 2021; Saikia et al., 2021a; 2021b), and seismicity (Schlaphorst et al., 2022).

Our study focuses on the Chain TF, which is characterized by a narrow 0 - 20 Myr old rupture zone, stretching over 300 km in roughly the east-west direction between two ridge spreading axes, slipping at a full spreading rate of ~30 mm/yr. Within the active fault zone, there are 4 lozenge shaped shallow bathymetric features, with en échelon fault scarps (Fig. 1). These features show evidence for reverse faulting in the sediments near the scarps, suggesting that these features are transpressional in nature. The features are interpreted as positive flower structures. The largest flower structure is located in the eastern Chain TF and is associated with a negative residual mantle Bouguer anomaly (rMBA). We refer to this structure as the eastern large flower structure (ELFS). The observed gravity anomaly at ELFS can be explained either by thicker crust or highly altered or damaged material (Harmon et al., 2018).

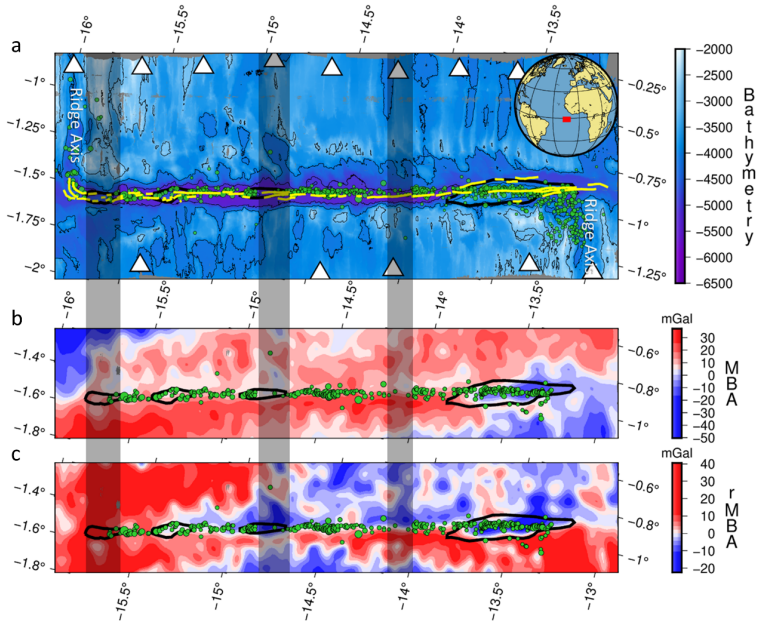

Figure 1. Geophysical features of Chain TF from Harmon et al. (2018) and all local seismicity located by Schlaphorst et al. (2022) presented as green circles. The locations of the closest OBS stations are represented by white triangles. (a) Bathymetric map of the study area with main faults (yellow curves) and flower structures (black curves). Bathymetry also delineates the ridge spreading centers that bound Chain, at the upper left and lower right parts of panel (a). The inset map at the upper right corner shows the location of Chain, marked by the red box. (b) Mantle Bouguer anomaly (MBA) in the study area. (c) Residual mantle Bouguer anomaly (rMBA) in the study area. Seismicity along Chain above completeness magnitude (M_C = 2.3), which was used for the analysis in this study is depicted as green circles in (b) and (c). The vertical shaded bars mark the location of the three OBS seismicity gaps.

In this study, we use the 1-year seismicity catalog presented in the work of Schlaphorst et al., (2022) and additional marine geophysical data gathered by the PI-LAB experiment (Harmon et al., 2018), focusing on the properties of seismicity of the Chain TF (Fig. 1). We investigate the space, time, and size distribution of seismicity along Chain TF and its connection to gravity anomalies and bathymetrical features. We perform cluster analysis in multi-dimensional phase space, consisting of various seismic and geophysical parameters. We then seek potential triggering mechanisms, including tidal effects, static and dynamic stress transfer. We extend our analysis in time by considering strong events (M_W 5.0) from the Global Centroid Moment Tensor (GCMT, Ekström et al., 2012). Finally, we extract information on the lithospheric structure and physical properties of the TFs by evaluating seismicity distribution, focal mechanisms and b-values, and integrating our results with previous findings.

1. **Materials and Methods**

   (a) **Seismicity Catalog**

We use the seismicity catalog compiled by Schlaphorst et al. (2022), containing 1492 events, 812 of which are located within the area surrounded by the OBS network, which belong to the Chain TF and the adjacent ridge spreading centers (Fig. 1b). In order to focus on the TF seismicity, we also discard the events that occurred unequivocally at the ridge segments and at the inside corners, based on their proximity to the spreading axis (10km) and available focal mechanisms. After this selection, 626 events remain along the Chain transform valley, detected from 13 March 2016 to 15 March 2017, characterized by a local magnitude (M_L) range between 1.1 and 5.4. The epicentral coordinates of these events are sufficiently constrained with median lateral uncertainties of 2.5 km. The vertical uncertainties are larger (median 18 km) with several events having uncertainties greater than 20km, at least for the entire catalog, regardless of quality. Given the large depth uncertainties for some of the events considered here, depth is not included as a parameter in the cluster analysis (see section 2.3). For 114 of these events focal mechanism solutions were derived, with 89 of them having good quality and depth determination, with mean vertical uncertainties of 6 km. Further analysis of those earthquakes, including their depths, can be found in the work of Schlaphorst et al. (2022).

Earthquake magnitudes are typically assumed to follow an exponential distribution, modelled by the Gutenberg-Richter law. Given the validity of exponentiality, the magnitude distribution above M_C, is parameterized by the well-known b-value, which can be evaluated by the Aki (1965) maximum likelihood estimator (MLE) as:

$$b = \frac{1}{\ln(10)(\langle M \rangle - (M_c - \frac{M}{2}))} \quad (1)$$

Where $\langle M \rangle$, is the sample mean of the events above M_C. The term $\Delta M/2$ accounts for the finite binning width correction of the magnitudes, which is equal to the round-off interval (0.1 in this study). Given N events with M M_C,

the standard error of equation (1) is estimated as (Aki, 1965):

$\sigma b = \frac{b}{\sqrt{N}}$ (2)

The Anderson-Darling Test (e.g., Marsaglia & Marsaglia, 2004; Leptokaropoulos, 2020) as well as the goodness of fit test (Wiemer & Wyss, 2000, modified by Leptokaropoulos et al., 2013) are performed to verify the exponentiality of the magnitude distribution and determine M_C. Both techniques return $M_C = 2.3$, suggesting that above this threshold the hypothesis of exponential magnitude distribution cannot be rejected at 0.05 significance. Therefore, the complete data for the study area (Fig. 1b, c) is comprised of 370 events with M_L 2.3 with a mean activity rate of ~1 event/day. The relatively small data size along with the considerable instability of the b-values calculated by MLE ($0.75 < b <$ 0.90 for 2.3 M_C 3.0) lead to large uncertainties and violate the unique b-value condition predicted by the GR law. Therefore, we applied the non-parametric, repeated medians technique (RM, Siegel, 1982) to evaluate the b-values, which has been shown to return more stable results and is highly resistant to the presence of outliers and uncertainties (Amorèse et al., 2010). Given n magnitude intervals between two points, i and j, we calculate n-1 slopes (b-values) between these points as:

$b_{ij} = \frac{\log_{10}(N_i) - \log_{10}(N_j)}{M_j - M_i}$ (3)

With M_j M_i. For each point, i, the median slopes (i.e., n median values) are calculated and consequently, b^{RM} is calculated as:

b^{RM}=-median(median(b_{ij})) (4)

The standard errors, SE, of the calculated b^{RM} are estimated by a bootstrap procedure as described in the work of Amorèse et al., (2010). The t-test is performed to evaluate the significance of whether the b-values from two datasets, e.g., A and B, differ from each other. The t statistic is defined as:

$t = \frac{|b_A^{RM} - b_B^{RM}|}{\sqrt{SE_A^2 + SE_B^2}}$ (5)

This approach results in b = 0.83 ± 0.09, with this value being practically unchanged regardless the applied magnitude cut-off value (b = 0.82 - 0.84 for 2.0 M_L 3.0). For this reason, we apply the RM approach to calculate all b-values in this study, with the corresponding SE, evaluated by 1,000,000 bootstrap resampling trials, unless stated otherwise.

The OBS network provides well-located seismic events but only covers a limited time period, and also does not include events larger than M_W ~ 5.5. To obtain better insights on how seismicity along Chain evolves within timescales of the order of decades, we use GCMT data, considering events with M_W 5.5 after 1976. For the events that occurred before 1976, there are considerable uncertainties in the epicentral locations (larger in latitude than in longitude), both relative and absolute. Pan et al. (2002) demonstrate that seismicity along the

MAR (30°S – 30°N) aligns well with the main active ridge or TF bathymetry, although a small number of lower magnitude events might be related to the secondary bathymetric features. Therefore, we proceed with our analysis under the assumption that all M_W 6.0 earthquakes considered in the study occurred along the Chain TF. For the most recent events that occurred after 1993, we use the relocated epicenters from Shi et al. (2021). Events before this time also have higher location uncertainties.

We integrated our local catalog with the available historical data (Fig. 2). In doing so, we make the following assumptions and assess their validity:

1. The M_L from the OBS catalog scales linearly with the M_w from GCMT.
2. Magnitude distribution obeys the same GR law for large (M_W 5.0, GMCT) as well as for smaller (2.3 M_L 5.0, OBS) earthquakes.
3. The overall magnitude distribution remains similar (sufficiently stable) from 1976 - 2021.

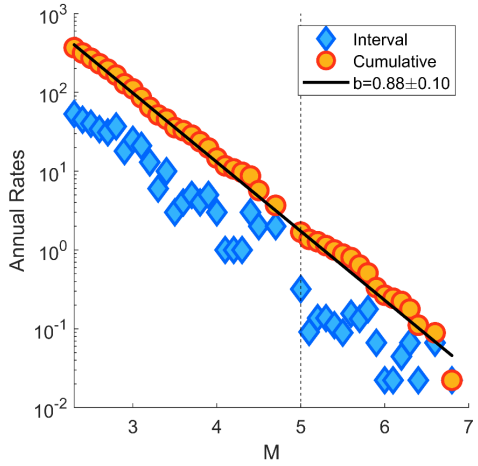

Figure 2. Interval (blue) and cumulative (yellow) annual frequency vs. magnitude for Chain TF. Data between 1976-2021 come from GCMT and data between March 2016 - March 2017 come from the OBS network (see text for temporal completeness levels). The solid black line indicates b = 0.88, whereas the vertical dashed line shows the transition from OBS (left) to GCMT data (right), around M = 5.0.

The completeness magnitude of the GCMT catalog for the study area is determined as a function of time. The AD-test is performed in various time windows and establishes that $M_C = 5.4$ for 1976-1999 and $M_C = 5.0$ after 2000. A total of 53 events from GCMT, satisfy the aforementioned conditions. The annual

rates of events considering these data are evaluated and then are merged with the OBS catalog (which corresponds directly to annual rates). There are 4 common events in the two catalogs, which have similar magnitudes (0.0 to 0.3 units difference). For these events we keep the M_L from the OBS catalog. In addition, the mean absolute difference in the longitude between OBS and GCMT for these 4 events is 0.05 °, whereas the corresponding mean latitude difference is 0.18 °. This suggests that although the CGMT epicentral locations have naturally larger uncertainties than OBS solutions, the longitude is sufficiently estimated and can be used as a good first order approximation. However, to have more precise locations for the along-strike variation of large events recorded since 1993 in our following analysis, we use the epicenters from the relocated catalog of Shi et al. (2021).

The annual event frequency of the merged catalog is shown in Figure 2. Overall, the data seem to obey the GR law with no visible changes in slope around M = 5.0, i.e., the transition from the OBS to the GCMT catalog. The RM technique returns b = 0.88 ± 0.10 for the merged catalog, which is close to the corresponding value from the OBS catalog, $b_{obs} = 0.83 \pm 0.09$. This provides an indication that that M_L scales linearly with M_W, thus the first two assumptions can be considered valid. There is a deficit of strong events at $M_W >$ ~6.5, which is typical for oceanic TFs (e. g., Boettcher & Jordan, 2004). Yet, the third assumption can be also considered valid, since the 45 year-period we took the data from should be representative of a complete seismic cycle, even in slow spreading oceanic ridge TFs (e.g., Aderhold & Abercrombie, 2016; Boettcher & McGuire, 2009).

1. **Ocean Tides**

Ocean tides are calculated by the SPOTL software (Agnew, 1997) considering the global ocean tide model TPXO72.2010, produced by Oregon State University (Egbert & Erofeeva, 2002). The tidal constituents M2, N2, S2, K2, K1, P1, O1, and Q1 are considered to calculate the predicted tidal heights (Agnew, 1997 and references therein) at the epicentral coordinates of each event for a 13h time span, centered at each event's occurrence time, with a time step for subsequent calculations equal to 72 seconds. By doing this we ensure that a complete semidiurnal tidal cycle (~12h 25min) is covered and a tidal phase within the cycle can be assigned to each event (Leptokaropoulos et al., 2021). We define the tidal phase, , relative to the low tide. In other words, 0° corresponds to the minimum water level, ± 90 ° correspond to zero tidal height, whereas +180 ° and -180 ° correspond to the subsequent and preceding high tides (maximum water level), respectively. After defining the phase of each event, we count the number of events that occurred at diverse phase bins to identify whether there is a preference for specific phase ranges. To quantify the significance of the results, we apply the Schuster (1897) test, calculating the probability, p, that the earthquake occurrence times introduced as tidal phase angles, are distributed around the unit circle in random occurrences. The parameter R, is thus defined as:

$$R^2 = \left(\sum_{i=1}^{N} \cos\phi_i\right)^2 + \left(\sum_{i=1}^{N} \sin\phi_i\right)^2 \quad (6)$$

with ϕ, being the tidal phase of the i^{th} earthquake in a population of N events. Then, the probability that a given tidal phase distribution is random is given by:

$$p_S = e^{-\frac{R^2}{N}} \quad (7)$$

Lower p_S values correspond to a higher significance of rejecting the null hypothesis of random phase distribution and vice versa.

1. **Cluster analysis**

Every seismic event can be represented by a point in a multi-dimensional space, quantified by a vector of values corresponding to parameters such as origin time, focal coordinates, magnitude, source dimensions, moment tensor components, etc. Studies of earthquake clustering typically consider distances between such points in multi-parameter spaces. However, the metric in such spaces cannot be readily defined, since different parameters demonstrate diverse ranges, distributions, and scaling. Transformation to Equivalent Dimension (ED) is a solution to this metric problem proposed by Lasocki (2014) based on the concept of probabilistic equivalence of continuous parameters. Following this approach, the lengths of parameter intervals are equivalent if the probability for earthquakes to take values from either interval is the same. Earthquake parameter distributions, which, in general, lack functional forms, are assessed using the non-parametric (data-driven) kernel estimation (Silverman 1986).

Let a seismic event be described by a set of continuous parameters X_i (X_1, …, X_n), with cumulative distribution functions of F_{X1}, … F_{Xn}, respectively. The ED of X_i is $U_i = Fx_i(X_i)$, with U_i uniformly distributed within [0, 1]. Each event is now parameterized by the $U(U_1,\ldots,U_n)$ vector in a n-dimensional space where the metric is Euclidean, such that the distance, D, between 2 events A and B can be defined as:

$$D(A,B) = \sqrt{\sum_{i=1}^{n} \left(X_i(A) - X_i(B)\right)^2} \quad (8)$$

After the transformation of seismic parameters into their ED, earthquake clustering is performed. We establish clusters in multi-dimensional space considering their linkage distance as derived by the hierarchical clustering approach introduced in the work of Ward (1963), which creates branches of interconnection among the points (earthquakes). This technique forms groups of mutually exclusive clusters until all clusters eventually join one group (event population). The degree of connection among individual events and the clusters that they gradually form is represented by a dendrogram. The linkage distance between

clusters, d(r,s) is specified as the average distance between all pairs of events in any of the clusters:

$d(r,s) = \frac{1}{n_r n_s} \sum_{i=1}^{n_r} \sum_{j=1}^{n_r} dist(x_{\mathrm{ri}}, x_{\mathrm{sj}})$ (9)

Note that this method does not require a predefined optimal number of clusters as, for example, the K-means algorithm does. This number can be determined based on an arbitrarily selected linkage distance, considering a trade-off between the number and size of clusters and their corresponding degree of interconnection. We perform cluster analysis in multi-dimensional space considering the following earthquake parameters (units in brackets):

- Longitude *[°N]*
- Latitude *[°E]*
- Local magnitude
- Tidal height *[m]*
- Mantle Bouguer Anomaly (MBA) *[mGal]*
- Residual Mantle Bouguer Anomaly (rMBA) *[mGal]*
- Bathymetry *[m]*

The latter three parameter values, originally estimated by Harmon et al. (2018) in a dense grid covering the study area, are assigned to each earthquake by nearest neighbor interpolation at the event epicenters.

1. **Dynamic Triggering**

We investigate the possibility of dynamic triggering by remote strong events (M_W 7.0) that occurred globally during the 1-year OBS deployment. 15 such events occurred, all located at epicentral distances greater than 50 °, with the exception of the 2016 August 29$^{\mathrm{th}}$, $M_W = 7.1$ event located at the nearby Romanche TF, a few hundred kilometres to the north-west of Chain. Remote triggering is statistically investigated by applying the binomial test on the seismicity rates along Chain, to search for significant rate changes possibly triggered by the passage of surface waves from teleseismic events. In doing so, we consider subsequent equal size time windows that range from 1 to 15 days before and after the occurrence time of each strong remote event. We test whether there is a significant increase in seismicity rates during one time window in comparison to the previous time window and also in comparison to the mean activity rate.

1. **Coseismic Static Stress Calculations**

We consider the potential static stress transfer from the $M_W = 7.1$ Romanche earthquake to the region along the Chain TF. Given that the Romanche is within a distance of a few fault lengths from Chain, it could potentially represent an important triggering factor (e.g., Harris, 1998). Coulomb failure function change (CFF) is calculated due to the coseismic displacement of the event.

The calculations are accomplished with the *Coulomb* software package (Toda et al., 2005; Lin & Stein, 2004):

$$\text{CFF} = + ' \, _{n} \quad (10)$$

where is the shear stress change, is the normal stress change, and ' the apparent coefficient of friction, including pore pressure effects and temporal changes of effective normal stress (e.g., Linker & Dieterich 1992). Failure is promoted when slip on the source faults induces positive CFF on the receiver faults. We applied a broad range of ' values ranging from 0.1 to 0.9 (see Results). The source fault dimensions are constrained horizontally by the aftershock sequence (L ~ 70km, Hicks et al., 2020) and vertically between the brittle-ductile transition assumed to be the 600° isotherm in a simple thermal model (~ 22km) (Abercrombie & Ekstrom, 2001; Hicks et al., 2020) and ocean bottom (~ 6km), given a very thin sediment layer of < 150m (Agius et al., 2018; Saikia et al., 2020). The rupture segment was considered to start from the eastern boundary of the TF with the mid-ocean spreading center, extending 70 km to the west across the transform zone. The published focal mechanisms for Romanche are very similar to each other and indicate an almost pure dextral rupture (176 ° rake) at a nearly vertical plane striking 79 ° and dipping 77 ° to the southeast (GCMT solution), defining a fault width, w = 16.5 km. The scalar moment, M_0, estimated by the same source is $5.7 \cdot 10^{19}$ Nm. The aforementioned fault dimensions and scalar moment combined with an assumed shear modulus, G, equal to 30 GPa (Olive & Escartín, 2017), results in a net slip, u = 1.6m (equation 11) which is almost exclusively concentrated along the strike direction.

$$M_0 = G \cdot L \cdot w \cdot u \quad (11)$$

We also calculate the potential static stress transfer from for the largest event recorded by the OBS during the deployment, a $M_L = 5.4$ that occurred on the western side of Chain TF, approximately 40 km from the ridge axis on October 27, 2016. We use the same assumptions applied to the Romanche stress transfer calculations with the following exceptions. The fault dimensions of the rupture area of the source fault are estimated from the scaling relations of Wells & Coppersmith (1994). In addition, the scalar seismic moment is obtained from the GCMT solution.

1. **Results**

   (a) **OBS seismicity cluster analysis**

The cluster analysis shows that distinct clusters are formed at different linkage distances, with four main clusters prevailing, as indicated in Figure 3. Although there is a small spatial overlap among the clusters, it is evident that Cluster 1 (108 events, blue) occupies the western part of Chain TF, Cluster 2 (126 events, orange) mostly covers the central part of the transform valley, whereas Cluster 3 (118 events, yellow) and Cluster 4 (18 events, purple) are located at the eastern part of Chain. Cluster 3 almost exclusively includes events within the ELFS, whereas Cluster 4 is located at the eastern tips and south of the ELFS. Due to

the small size of Cluster 4 (18 events) and its spatial proximity to Cluster 3, we decided to merge these two clusters, hereinafter referred to as Cluster 3/4. The inset at the bottom of Figure 3 shows the interrelation dendrogram formed by the 370 events with M_L 2.3, comprising the complete data obtained from the OBS network. Note that the dendrogram indicates that Cluster 1 and Cluster 2 are more closely linked with each other in the 7-dimension space than Cluster 3 and Cluster 4. In addition, some of the Cluster 4 events are located at the core complex rather than at the transform. For this reason, we also present the results for Cluster 3 alone, simply discarding the 18 events of Cluster 4 from the analysis, although the results remain essentially similar (Table 1).

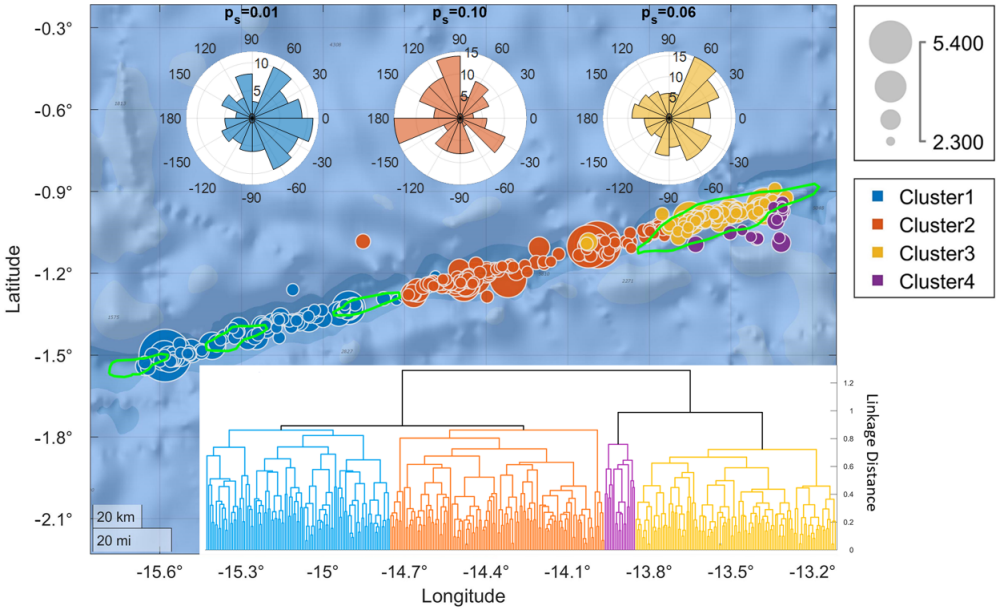

Figure 3. Spatial distribution of the 4 major clusters derived by the hierarchical cluster analysis. The inset at the lower part of the figure presents the dendrogram showing the interconnection among the earthquakes, ultimately forming a tree. The lower the branches meet with each other the stronger the clustering. Linkage distance is indicated at the y-axis on the right. The colors in the dendrogram correspond to the colors of the clusters in the map and the circles' size is proportional to the event magnitudes (2.3 M_L 5.4). The polar histograms at the top of the figure show the tidal phase distribution for each cluster (from left to right, Cluster 1, Cluster 2, Cluster 3, indicated by the respective colors) and the corresponding Schuster test p-value, p_s. The green curves delineate the four positive flower structures.

Table 1 shows an overview of seismic and geophysical parameters that characterize the 3 dominant clusters. The distributions of magnitudes, bathymetry, MBA and rMBA are shown in Figure 4. Figure 4a shows the cumulative mag-

nitude distribution of the three clusters. Cluster 1 and Cluster 3 have similar magnitude distributions, with Cluster 1 including more events with $M_L > 3.0$ than Cluster 3. In addition, the largest event in the catalog ($M_L = 5.4$) belongs to Cluster 1, leading to a lower b = 0.91 ± 0.15, in comparison with b = 0.97 ± 0.18 estimated for Cluster 3, although the two are not statistically different from one another. On the other hand, Cluster 2 contains a considerably higher number of larger events ($M_L > 3.5$), compared to the other two clusters, evident by a characteristic change of slope in the cumulative distribution above this magnitude threshold. Consequently, the b-value of Cluster 2 equals 0.71 ± 0.13, considerably lower than the b-values of Clusters 1 and 3. However, the total seismic moment release, M_0, (derived as in Hanks & Kanamori, 1979) is roughly equal for Cluster 1 and Cluster 2 (~1.5 10^{17} Nm), being ~6 times higher than the M_0 released by Cluster 3/4. This means that although seismicity rates are much higher at the ELFS, this part of Chain contributes only a small proportion of the total seismically released energy. The closer connection between Clusters 1 and Cluster 2 in the 7-dimensional space, compared to Cluster 3/4, is evident by the distributions of MBA, rMBA and bathymetry values (Table 1; Fig. 4b, 4c and 4d, respectively). Events belonging to Cluster 3/4 have the lowest values in all three aforementioned parameters, generally corresponding to negative MBA and rMBA values, and a mean ocean depth of 3800-3850 m, depending on whether the events from Cluster 4 are included. Clusters 1 and 2 are associated with deeper bathymetry (~5300 m and 5100 m, respectively), whereas they both have positive mean MBA, somewhat higher for Cluster 2 (Table 1). Both Clusters 1 and 2 show close to zero mean rMBA values (Table 1). However, Cluster 1 has a bimodal distribution with two local maxima around -5 mgal and +5 mgal (Fig. 4c). Finally, the tidal phase diagrams are shown in the upper inset of Figure 3. The tidal height associated with the occurrence time of the events, is shifted towards low tides (0 °) for Cluster 1 and Cluster 3, and slightly shifted towards high tides for Cluster 2 (180 °) (Table 1). This indicates a minor preference for events occurring at low tides (tidal phase between -90° to 90°) closer to the two edges of Chain.

Table 1. Summary of the properties of the main clusters derived by multidimensional cluster analysis (shown in Fig. 3). The columns indicate subsequently: The Cluster ID; the number of events, N; the b-value; the total seismic moment release, M_0; the mean bathymetry; the mean MBA; the mean rMBA; the median tidal height, with negative and positive values corresponding to low and high tides, respectively; the p-value of the Schuster test, p_s. The numbers following the ± symbol, indicate one standard deviation.

Cluster ID	N	b-value	M_0 (10^{17} Nm)	Bathymetry (m)	MBA (mgal)	rMBA (mgal)	Tidal Height (cm)	p_s
Cl. 1		±0.12		±255	±2.7	±4.9	±33.3	
Cl. 2		±0.13		±274	±3.1	±3.3	±30.0	
Cl. 3		±0.18		±373	±6.0	±3.1	±3.1	

Cluster ID	N	b-value	M_0 (10^{17} Nm)	Bathymetry (m)	MBA (mgal)	rMBA (mgal)	Tidal Height (cm)	p_s
Cl. 3/4		±0.18		±433	±6.5	±7.4	±3.0	

We further investigate the magnitude distribution dependence on individual parameters. In doing so, we consider MBA, rMBA, bathymetry and tidal height values, sorted in an ascending order and then we calculate b-values and their standard error with the RM technique. After performing calculations for different sliding windows consisting of 50, 75, 100 and 125 events, advancing by 1 event, we obtained similar results. We therefore present the results for 100-event windows (Fig. 5). Figure 5a shows b-value fluctuations with MBA. Apart from some relatively elevated b-values for MBA $<$ ~-3 mgal, no remarkable variations are evident throughout the MBA range. Negative MBA values are almost exclusively met beneath the ELFS, where the shallowest bathymetry is observed. The rMBA plot shows two distinct domains divided at rMBA ~ -3 mgal (Fig. 5b). Event windows with rMBA $<$ -3 mgal have larger b-values than event windows with rMBA $>$- 3mgal. Division of data in two equally sized groups, suggests that events located at areas with rMBA $<$ -3mgal have b = 1.04 ± 0.13, and events located at areas with rMBA $>$ -3mgal have b = 0.72 ± 0.11. This b-value difference between the two datasets is statistically significant at 0.05 level (the t-statistic values is 1.96, equation 5). A relationship between magnitude distribution and bathymetry is indicated in Figure 5c, where b-values gradually decline with increasing ocean depth. The shallower depths are generally related to higher b-values in comparison to the areas with deeper bathymetry. If we divide the data into 3 evenly sized, nonoverlapping datasets, the resulting b-values are 0.94 ± 0.19, 0.86 ± 0.17 and 0.78 ± 0.09 for shallow, intermediate and deep bathymetry, respectively. These values present considerable overlap with each other and they clearly do not suggest a significant difference. However, they offer a rough view on the b-value distribution connected with bathymetry. A not so clear linear trend is observed in the tidal height plot (Fig. 5d), with b-values seeming to monotonically increase for tidal heights between -0.2 m and 0.2 m. In general, earthquakes occurring at positive ocean heights (high tides) appear to demonstrate higher b-values than the ones that occur at negative ocean heights (low tides). A possible sinusoidal relation is also visible, although the uncertainties are too large to verify the significance of a sinusoidal shape.

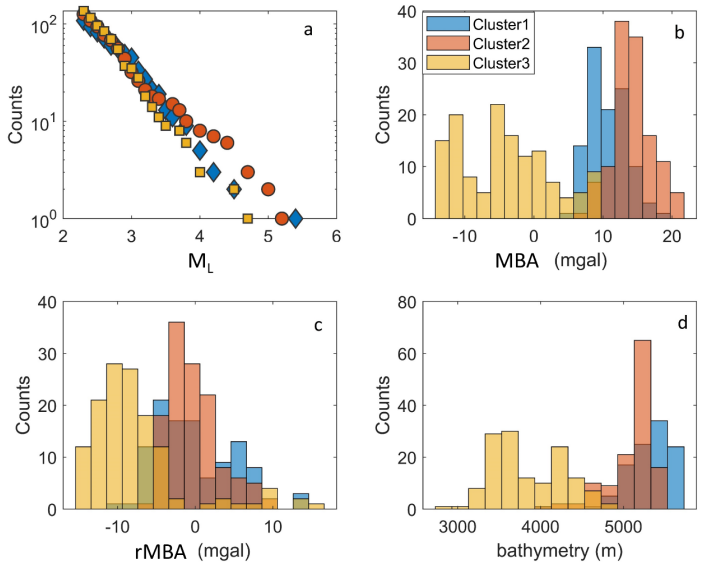

Figure 4. Value ranges of each parameter for Cluster 1 (blue), Cluster 2 (red) and Cluster 3/4 (yellow). The corresponding parameters are labelled in the x-axis: (a) M_L, (b) MBA, (c) rMBA, (d) Bathymetry. Note that the cluster analysis has been carried out in the equivalent dimensions, whereas these histograms represent the values in the original dimensions.

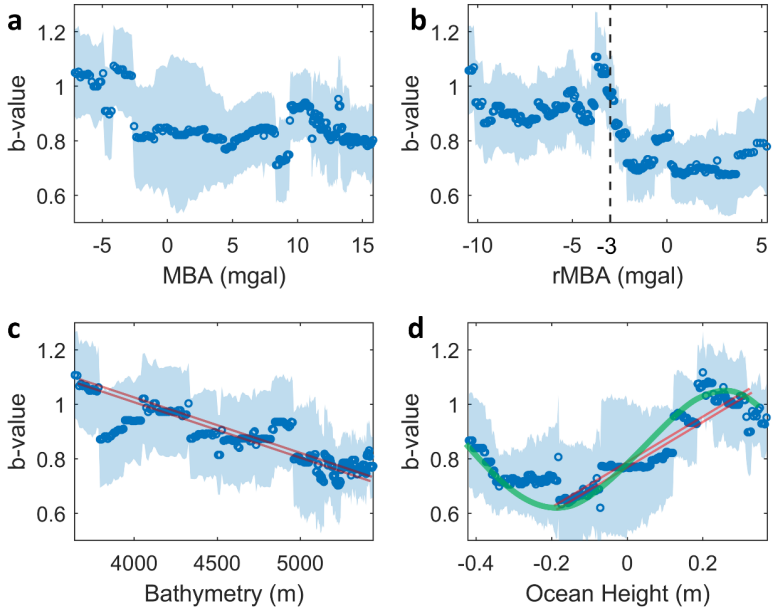

Figure 5. Single-parameter influence on magnitude distribution: (a) MBA (mgal), (b) rMBA (mgal), (c) bathymetry (m) and (d) ocean height (m). The blue dots show the b-values estimated by the repeated median technique for 100-event windows, plotted in the center of each window. The windows are shifted by 1 event after each calculation. The shaded areas show the bootstrap standard error of b-value estimation, derived by 1,000 resamplings. The vertical dashed line in (b) indicates the -3 mgal threshold, dividing the data into high ($<$ -3 mgal) and low ($>$ -3 mgal) b-values, respectively. The red lines in (c) and (d) show average linear trends, whereas the green line in (d) indicates a sinusoidal approximation with peaks at approximately $\pm$ 0.20 m.

1. **Spatio-temporal seismicity variations from OBS and historical data**

Following the results of the cluster analysis we divide the Chain TF into 3 areas: western, central and eastern areas (W, C and E in Fig. 6, respectively), having well-defined although slightly overlapping borders. The average OBS seismicity rate is not equally distributed along the TF strike (Fig. 6, Table 2). The first characteristic is that seismicity rates become higher from the west to the east, as suggested by the number of events per longitude degree (Table 2). The eastern area demonstrates 3 and 2 times higher activity rates compared to central and western areas, respectively. There is a narrow Transition Zone (TZ in Fig. 6) of ~25 km, overlapping between Cluster 1 and Cluster 2, where there are 62 events (19 from Cluster 1 and 43 from Cluster 2). Cluster 1 is also defined by the existence of the 3 westernmost flower structures, and it contains less events in the transition zone. For these reasons we divided western and central areas at -14.68° longitude. There is also a very narrow zone between Cluster 2 and Cluster 3, including only 3 events from Cluster 3. For the same reasons, we divided central and eastern areas at -13.76° longitude. There are 3 characteristic spatio-temporal OBS seismicity gaps (purple shades zones, g1, g2, g3, Fig. 6). OBS seismicity gaps are defined as areas where the seismicity rate drops below a specified level. We calculate the average OBS rate equal to 150 events (M_L 2.3) per longitude degree (/ °). We then define a seismicity gap when the rate falls below one fifth of the average rate (30 events/ °) for a length of at least 0.15 ° or ~15 km (arbitrary selection). Gap g1 (~ 40 km length) is located at the same location as the westernmost flower structure and is characterized by an almost complete absence of events (3 events, 1 above $M_C = 2.3$) for at least 7 months before the occurrence of the October 27, 2016, $M_L = 5.4$, which was the strongest event recorded by the OBS network. 4 events above M_C are found in gap g2 (~ 20km length) which is located at the easternmost part of the western area. This gap overlaps substantially with the easternmost flower structure in the western segment of the TF. 3 events above $M_C = 2.3$ occurred in gap g3 (~ 15km length), which is located close to the middle of the central area. Gaps g2 and g3 persist for the entire duration of the OBS network.

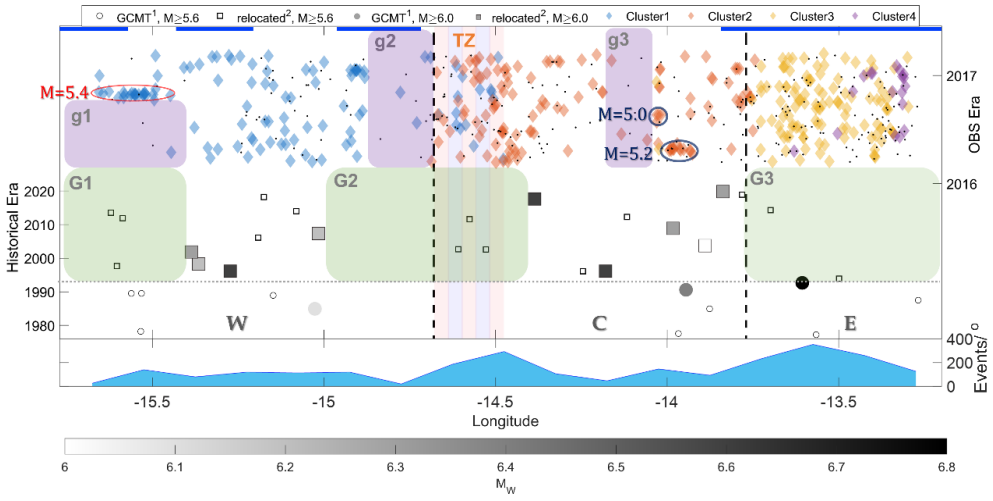

Figure 6. Longitude-Date summation, integrating the data and results from OBS seismicity analysis (upper part, right y-axis) and global CMT data (lower part, left y-axis). The 4 Clusters in which OBS data were grouped are shown as colored diamonds (see legend for details) and comprise only the complete data with M_L 2.3. The dots indicate the remaining microseismicity events with $M_L < 2.3$. The purple-shaded boxes denote the location of OBS seismicity gaps (g1, g2, g3). The transition zone (TZ) between Cluster 1 and Cluster 2 (see text for details) is shown by the colored vertical bars. Squares denote the relocated data from Shi et al. (2021) for events after 1993, whereas circles indicate the locations reported by GCMT for events before 1993. Grey-filled symbols represent the strongest (M_W 6.0) events that occurred since 1976, with the color scale beneath the plot indicating the magnitudes. Open symbols show the events with 5.5 $M_W < 6.0$. The green-shaded boxes denote the location of historical seismicity gaps (G1, G2, G3), i.e., areas with absence of M_W 6.0 events since 1993. The temporal extent of the Shi et al., (2021) catalog (1993) is indicated by the dotted horizontal line. The blue horizontal lines just below the legend indicate the location of the flower structures. The dashed vertical lines divide Chain into three areas, Western (W), Central (C) and Eastern (E). The red and blue ellipses indicate the extent of the seismic activity related with the 3 strongest (M_L 5.0) events along Chain, which are marked by the yellow stars. The blue area at the bottom of the figure shows the moving mean OBS seismicity rate for non-overlapping bins with 0.15 ° length.

Table 2. Summary of the properties of seismicity (from OBS and GCMT) in the three areas, as derived by multidimensional cluster analysis (shown in Fig. 3). N, is the number of events, b, is the GR law b-value, and M_0, is the seismic moment. Apart from the b-values, all the other parameters are normalized by longitude unit.

	Western Area	Central Area	Eastern Area
Longitude	-15.65° to -14.68°	-14.68° to -13.76°	-13.76° to -13.29°
$N_{obs}/°$ ($M_L > 2.3$)	98	148	296
$N_{GCMT}/°$ (M_W 5.5)	19.6	16.3	10.6
b_{obs}	0.89±0.12	0.74±0.13	0.98±0.15
b_{merged}	0.91±0.12	0.83±0.19	1.04±0.13
$M_{o(OBS)}/°$	1.88 10^{17}	1.74 10^{17}	0.64 10^{17}
$M_{o(GCMT\_1993)}/°$	2.35 10^{19}	3.47 10^{19}	0.19 10^{19}

The strongest M_W 6 events after 1993 (filled squares, Fig. 6) are also not uniformly distributed. 4 of them are located at the center of the western area, and 5 of them are located at the mid-eastern part of the central area. The existence of seismic gaps is shown for the historical data as the green shaded zones (G1, G2, G3, Fig. 6). We define historical seismicity gaps as areas with lengths greater than 30km, a length which could potentially rupture a roughly M_W=6.6 earthquake (Wells and Coppersmith, 1994), but where no events M_W 6.0 have been recorded since 1993. Gap G1 (~40 km length), coincides spatially with OBS seismicity gap g1, and is characterized by an episodic occurrence of events with 5.6 $M_W < 6.0$, approximately at the location of the October 27, 2016, $M_L = 5.4$ event recorded by the OBS network. Two large gaps (~65 km length) are also present. Gap G2 occupies parts of the western and central areas. Only three events with 5.6 $M_W < 6.0$ have occurred since 1993, whereas no M_W 5.6 has been recorded within over 40 km. Gap G3 essentially covers all the eastern area beneath the ELFS, where only 2 events with 5.6 $M_W < 6.0$ have occurred since 1993. There is one strong event ($M_W = 6.8$) in the GCMT catalog. However, the reported epicenter has not been relocated, therefore there may be considerable location uncertainty. It is worth noting that the gaps determined by the long-term data are not always consistent with the OBS seismicity gaps. However, nearly all M_W 6.0 events occur at patches with moderate to small OBS seismicity rates (90-120 events/ °) and the segments with the highest OBS seismic activity (>250 events/ °) are characterized as gaps (no events with M_W 6.0) by the long- term data (e.g., ELFS, central Chain) (Fig. 6).

The b-values are generally consistent with each other when considering the OBS data alone and the merged catalog (Table 2). The central area (Cluster 2) demonstrates the lowest b-values (b ~ 0.70-0.80), although the difference from the other Clusters is not statistically significant. The highest b-values are evident in the eastern area along the ELFS (b ~ 1.0), where OBS seismicity rates are the highest. The seismic moment release, M_0, (normalized by longitude unit) from the OBS catalog is similar for the western and central areas (44 % - 41 % of the total potential seismic moment release, respectively), being almost 3 times higher than in eastern area (15 % of the total seismic moment). When the merged catalog after 1993 is considered, 58% of the total potential seismic moment is released in the central area, 39% in the western area, and only 3% in the eastern area.

1. Potential triggering mechanisms

(a) Dynamic triggering

Figure 7 shows a plot with seismicity rates averaged over 15-day windows. All window bands tested (1 – 15 days), revealed 3 periods of significant rate increase at 0.05 level (grey-shaded areas in Fig. 7), compared to the average seismicity rate from the 1-year period (1 event/day). The first two periods of increased activity rate (19 – 30 April, 2016 and 10 October - 7 November, 2016), coincide with the occurrence of the two strongest events in our OBS catalog (27 April, 2016, M_L = 5.2 and 27 October, 2016, M_L = 5.4, left and right green stars, Fig. 7), respectively and they are mostly locally distributed in the close vicinity of these events (Fig. 6). The third period of enhanced seismic activity, which takes place on January 2017, is not connected to a particular large, local event. The local M_W = 5.0 event that occurred on August 20th, but did not cause a remarkable aftershock sequence (middle green star, Fig. 7).

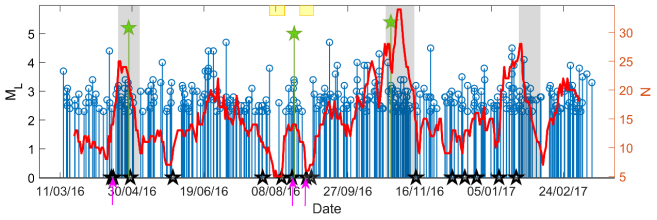

Figure 7. Seismicity stem plot (blue) and number of events that occurred in subsequent 15-day windows (continuous red curve), with each point plotted at the first event of the corresponding period. The mean event count from all 15-day periods is 15 events, and N 25 (right y-axis), indicates a significant rate change at 0.05 level according to the binomial test. Three such periods are identified, shown within the vertical shaded bars. The black stars in the x-axis depict the occurrence time of 15 remote M_W 7.0 events. The green stars indicate the three largest events on the Chain Fracture Zone recorded by our array (from left to right, 27th April 2016, M = 5.2; 20th August 2016, M = 5.0; 27th October 2016, M = 5.4, see text for details). The magenta arrows indicate the three remote events that are described in the text and are not likely associated with dynamic triggering. The yellow boxes indicate the two weekly periods of quiescence (see text).

No strong global event coincides with the aforementioned dates of heightened OBS seismicity, with the exception of an M_W = 7.8 earthquake that occurred in Ecuador on 16 of April 2016 (left magenta arrow, Fig. 7). It occurred three days before the beginning of the 19 – 30 April sequence, which culminated with the

5.2 event on the 27th of April and seized soon after (only four events followed the next week). The large epicentral distance of the $M_W = 7.8$ event from Chain ($\sim 65°$) together with the almost 3 days delay of the initiation of the swarm, strongly oppose the dynamic triggering hypothesis (e.g., Gomberg et al., 2004).

One other potential triggering case is connected to the $M_W = 7.5$ event that occurred on 2016, August 19th, in the South Georgia Island region (middle magenta arrow, Fig. 7), which occurred ~36 hours before the occurrence of the 20th August, $M_L = 5.0$ event, although no significant increase in seismicity rate was detected. Thus, there is probably no causative effect, taking into account the long distance of the event (> 6000 km) and the small available sample for a robust statistical evaluation (~12 OBS events in 10 days period, centered on the South Georgia event's origin time).

No influence from the close Romanche event ($M_W = 7.1$, 29th August 2016, right magenta arrow) on seismicity rates on Chain TZ are observed, with seismic activity remaining almost stable within 15 days before and after its occurrence. However, there was an aftershock series on Romanche (Hicks et al., 2020). It is also worth noting the presence of two nearly week-long periods of complete seismic quiescence, on 3 - 10 August 2016 and 26 August – 2 September 2016 (yellow bars in Fig. 7).

Overall, the one-year of data recorded by the OBS network revealed no clear evidence of dynamic triggering from remote events. The seismicity analysis demonstrates a stable activity in terms of seismicity rates (1 ± 0.36 events/day), with only some degree of temporal fluctuations, i.e., two weekly gaps and three periods of increased rates, two of them coinciding with the 2 strongest local events ($M_L = 5.2$ and $M_L = 5.4$).

1. **Static stress triggering**

Following the absence of an apparent dynamic seismicity response from remote events and the regional event at Romanche we investigate the potential static stress triggering from the Romanche event and the largest event (M_L=5.4) on Chain.

Figure 8a shows the coseismic CFF due to the $M_W = 7.1$ Romanche event resolved onto the fault plane of the strongest event of the OBS dataset, the October 27th 2016, $M_L = 5.4$ event with 249 °/261 ° strike, 73 °/76 ° dip, 176 °/168 ° rake (Schlaphorst et al. 2022; Global CMT: Ekström et al., 2012). Note the similarity between the focal mechanisms of the source (79 °/77 °/176 °) and the receiver faults, which are typical right lateral mechanisms for the two oceanic transform systems. The positive and negative CFF lobes are shown at the depth of 16 km below sea level (~10 km within the oceanic lithosphere), assuming a friction coefficient, = 0.4 (Deng and Sykes, 1997; Parsons et al., 1999). Chain falls in the negative lobe, where triggering is not enhanced.

Figure 8b shows the corresponding CFF caused by the occurrence of the M_L = 5.4 Chain event resolved onto the same fault plane. The color scale has

been saturated at ± 0.1 bar, which is a commonly accepted CFF threshold for regions capable of promoting or (debatably) inhibiting seismicity rates (e. g., Stein, 1999; Scholz et al., 2019). The $M_L = 5.4$ event on Chain (Fig. 8b) induced stress changes with amplitudes capable of influencing seismic activity rates only in the very close vicinity of the source fault (~ 15 km away from the fault edges). Such stress variation cannot cause sufficient changes to seismicity rates across the broader Chain TF. Moreover, due to the narrow ΔCFF lobes and the small number of events, it is not possible to robustly quantify the stress change effect on seismicity, although Coulomb stress transfer is a rather plausible triggering factor of the aftershock sequence following the $M_L = 5.4$ event (right green star, Fig. 7).

The stress pattern shown in Figure 8a remains stable regardless of the friction coefficients that are assumed (from 0.1 to 0.9) and in most cases the seismicity across Chain is found within the negative lobe, i.e., where triggering is not enhanced. For values higher than 0.75 the westernmost part of Chain TF is located in positive CFF area. However, the predicted stress changes are lower than the 0.1 bar threshold. The coefficient of friction for the serpentine polymorph, lizardite, which is the most abundant form in the oceanic lithosphere, is μ ~ 0.35 (Escartín et al., 1997), reaching ~ 0.5 at high temperatures (Moore et al., 1997). In addition, even slightly serpentinized peridotites show a similar behavior to that of pure serpentinite (Escartín et al., 2001). Moreover, the intrinsically lowered brittle strength of even slightly serpentinized peridotite compared to the typical fractured lithospheric rocks creates suitable conditions for an additional decrease in the effective friction coefficient due to the presence of fluids under pressure (e.g., Dymkova & Gerya, 2013). It is therefore expected that the friction coefficient should be substantially below 0.75.

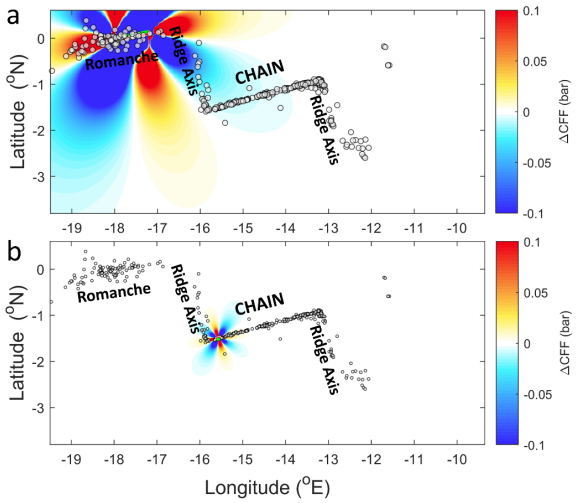

Figure 8. CFF variation caused by a) the $M_W = 7.1$ event (Romanche TF) and b) the $M_L = 5.4$ event (Chain TF). Warm colors represent positive CFF,

whereas cold colors correspond to negative CFF. The circles indicate the epicenters of earthquakes with M_L 2.3 that occurred across the two transform systems and the adjacent ridge spreading centers during the operation of the PI-LAB network (Schlaphorst et al., 2022). The map boundaries and color scales are identical for comparison.

1. **Tidal triggering**

There is some evidence of weak ocean tidal triggering for Cluster 1 and Cluster 3 (western and eastern areas). The majority of the events (Fig. 3, inset polar histograms) from the complete catalog occurred during low tides which have been shown to promote slip in the reverse faulting regime (e.g., Wilcock, 2009), providing there is a considerable vertical component in the focal mechanism of the source. Although the Schuster test confirms this hypothesis (for M_L 2.3) at 0.01 and 0.06 significance levels for Cluster 1 and Cluster 3, respectively, cluster analysis includes tidal height as one of the seven earthquake parameters used and therefore, some degree of bias is introduced in the resulting clusters. To eliminate this influence, we further perform Cluster analysis in 6-dimensional phase space, discarding tidal height from the procedure. This leads to a small redistribution of events between Cluster 1 and Cluster 2, whereas Cluster 3 and Cluster 4 remain essentially intact. Tidal triggering is no longer detected for the first two Clusters (regardless of the magnitude threshold chosen). Nevertheless, the Schuster test for Cluster 3 returns $p_s = 0.04$, indicating a relative preference of M_L 2.3 events that occur during low tides. This may indicate that a non-negligible vertical component is included in the focal mechanism of events at the easternmost side of Chain, plausibly related with the ELFS. To test this hypothesis, we consider the available focal mechanisms for the study area. All M_L 6.0 and the vast majority of the reported GCMT solutions suggest strike-slip faulting along Chain TF. However, OBS seismicity focal mechanism analysis reveals that a small number of events demonstrate a considerable vertical component (mostly reverse, with a few events having normal component). We invert the local stress field from the available focal mechanisms using the *stressinverse* software (Vavryčuk, 2014) to calculate the orientation of the maximum ($_1$), intermediate ($_2$) and minimum ($_3$) principal stresses together with the shape ratio, R. R takes values between 0 and 1, and it determines the relative amplitudes of the three principal stresses. An R value closer to 0 indicates that $_1$ and $_2$ have similar amplitudes. R values closer to 1 indicate that $_2$ and $_3$ have similar amplitudes. R values close to 0.5 show a clear difference among the principal stress amplitudes. Due to the limited number of focal mechanism solutions (114), we divide the data into two equally sized groups (57 mechanisms each), corresponding to the western and eastern half of Chain. In both cases $_1$ is horizontal or nearly horizontal trending towards the SE-NW direction. For the eastern part of Chain (Fig. 9a, b) the distribution of the $_2$ and $_3$, along with the high shape ratio value (0.87) provide a strong indication that the intermediate and minimum principal axes are virtually indistinguishable from each other. Under such conditions the simultaneous activation of both reverse and strike-slip faults are plausible (e.g., Fojtíková & Vavryčuk, 2018; Hallo et al.,

2019). For the western part of Chain (Fig. 9c, d) there is also no unequivocal vertical principal stress, although the plunge of $_2$ is a somewhat steeper that $_3$ (52 °, and 32 °, respectively). The shape ratio also has a relatively high value (0.79), indicating that transpressional features may be present in the western half as well, although they are less pronounced in comparison to the eastern half (including the ELFS).

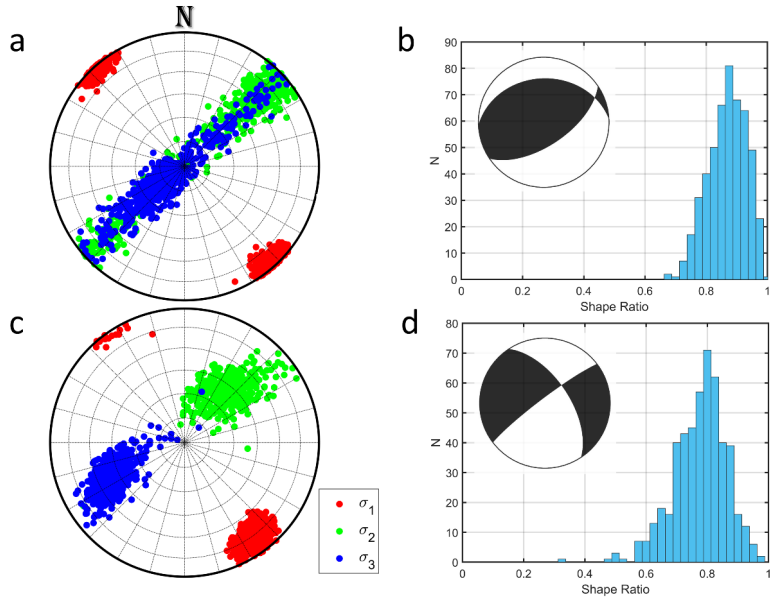

Figure 9. Stress inversion results for the eastern (a, b) and western (c, d) halves of Chain TF. (a) and (c) show the distribution of the confidence intervals of principal axes' orientation, obtained by 500 realizations. The radii indicate the direction of the azimuth, with 0 ° corresponding to north, as indicated by N, in panel (a). The concentric circles denote the plunge, with the center indicating vertical direction (90 °) and the outer circle indicating horizontal direction (0 °). Panels (b) and (d) show the histogram of the shape ratio values, also derived from 500 realizations. The inset beachballs in (b) and (d) show the average focal mechanism for the eastern (strike=254 °, dip=33 °, rake=116 °) and the western (strike=313 °, dip=60 °, rake=-173 °) halves of Chain TF, respectively.

1. **Discussion**

The generally low average b-values along Chain (~0.85) provide evidence of relatively high seismic coupling, defined as the area displaced by seismic slip divided by the thermally constrained seismogenic area. This agrees with estimates of theoretical versus observed seismic moment release which suggests that the seismic coupling coefficient in Chain equals ~1/3 (Wolfson-Schwehr & Boettcher, 2019), which is among the highest values in MAR (0.85 quantile).

There does not appear to be evidence for large repeating earthquakes along

Chain TF. No $M_W > 7.0$ events rupturing the entire TF have been recorded. No quasi-periodical earthquake cycle is evident for M_W 6.0 events along Chain for over 30 years. This is different from other transforms such as the Charlie-Gibbs TF (north Atlantic), which has strong earthquakes (M_W~7.0) that occur quasi-periodically (Aderhold & Abercrombie, 2016).

The historical teleseismic dataset indicates high lateral heterogeneity in seismicity along Chain. There is a long-term absence of strong events within three gaps (G1, G2, G3, Fig. 6). We observe two locked patches (asperities), with total length ~50 km and ~75 km, respectively, which have repeatedly ruptured $M_W > 6.0$ earthquakes (Fig. 6).

Lateral heterogeneity is also inferred from the OBS data. Our multi-dimensional cluster analysis of OBS seismicity, divides the TF into 3 slightly overlapping, yet distinct areas with diverse properties (eastern, central, western). The gaps in OBS seismicity (g1, g2, g3, Fig. 6) do not necessarily occur in the same locations at those in the teleseismic records, although areas with intermediate to low OBS seismicity rates (~100 events/ °) occur in regions where teleseismic $M_W > 6.0$ earthquakes tend to occur. For comparison, the average OBS activity rate along Chain is 150 events/ ° (see also Table 2 and Fig. 6).

The observed transform segmentation along Chain (3 areas) is in general agreement with the conceptual models of Boettcher & Jordan (2004). In these models the seismogenic zone is divided into multiple patches, such that either brittle (purely coupled), ductile (purely aseismic), or time-dependent (semi-brittle) deformation applies. The eastern area is characterized by the presence of ELFS, negative rMBA, abundant OBS seismicity, but negligible seismic moment release, evidenced by the historical data. Negative rMBA areas are explained by mass deficit, likely caused by thicker crust and/or hydrothermal alteration. This area is also accompanied by higher b-values, consistent with weaker coupling (i.e., less brittle behavior). The negative rMBA combined with the shallowest bathymetry occurring beneath at ELFS, likely suggests that the crust is thicker by up to 1 km or has an altered mantle with lower densities (Harmon et al., 2018). Our stress inversion results (Fig. 9) agree with the notion of transpression in the region, particularly beneath ELFS, as suggested by previous morphological studies (Harmon et al., 2018).

In contrast to the ELFS, the western and central areas exhibit positive rMBA, lower OBS seismicity rates (3 and 2 times lower than the eastern area, respectively), but they accommodate almost the entire long-term moment released seismically (>97%). Positive rMBA anomalies require mass excesses. This can be explained by thinned crust and/or a lack of hydrothermal alteration. These regions are also associated with lower b-values, indicative of greater coupling and more brittle behavior.

The lateral variability of frictional response is likely caused by some combination of the rock composition, stress/temperature conditions, fault geometry, and/or hydrothermal alteration (e. g., Roland et al., 2010, 2012; Liu et al., 2012;

Wolfson-Schwehr et al., 2014). Deeper, in the oceanic mantle water can substantially weaken olivine (Kohli et al., 2021) by enhancing dislocation and diffusion creep mechanisms (Karato et al., 1986). It is also likely that the mafic crust contains pockets of serpentinite (barriers), resulting from tectonism or/and fluid flow through the fractured material (Gregory et al., 2021). Conversely, asperities may be caused by dry patches (inaccessible to water) or patches where there is an absence of serpentine.

No remote dynamic stress triggering was identified. Static stress triggering was possibly caused by three 5.0 M_L 5.4 along Chain. The 27 April 2016, M_L = 5.2, was preceded by 8 M_L 2.3 events in the week before and was followed by 3 M_L 2.3 events in the week after the main shock occurrence. The 20 August 2016, M_L = 5.0 earthquake had no precursors in the week before and was followed by 3 M_L 2.3 events in the week after the main shock occurrence. These two mainshocks had similar size and occurred at the western tip of the eastern area at approximately the same location (Fig. 6, Fig. 10). However, they demonstrate diverse foreshock activity and a negligible aftershock sequence. The 27 October 2016, M_L = 5.4 event was preceded by only two, yet relatively strong events (M_L 4.0) in the week before and was followed by 13 M_L 2.3 events in the week after the main shock occurrence, indicating a rather weak mainshock-aftershock sequence. These cases agree with the notion that mainshock-aftershock sequences are not common for oceanic TF earthquakes (e.g., Scholz, 2019). Our results are also consistent with the global perspective, showing that the number of aftershocks at oceanic TF are typically ~1 order of magnitude fewer than continental earthquakes, possibly due to the much slower rate of static fatigue of gabbro compared to granite (Meredith & Atkinson, 1985) and the existence of serpentine phases.

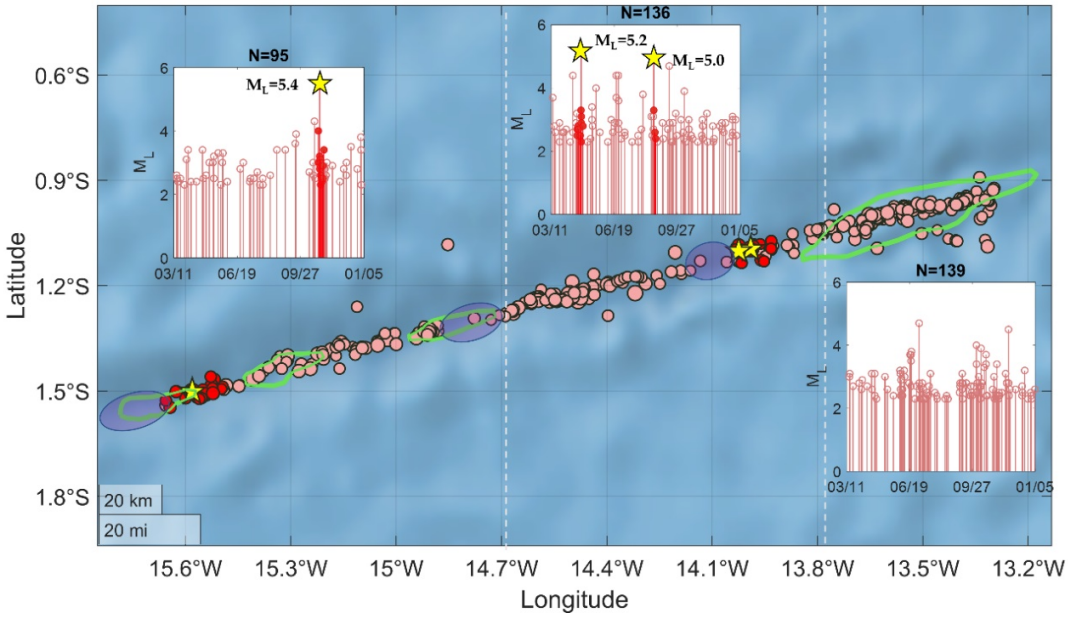

Figure 10. Seismicity above $M_C = 2.3$ (pink dots) along Chain, delineates 3 distinct segments (Western, Central, Eastern, separated by the vertical dashed lines), as derived by the cluster analysis. Seismicity gaps, i.e., areas with sparse OBS seismicity are indicated by the purple ellipses. The red dots indicate the seismicity that occurred 1 week before and 1 week after the three strongest events (M_L 5.0, depicted by yellow stars). The inset stem plots show the temporal distribution of events' occurrence times for each area, with their corresponding order (from left to right), with the data highlighted in red corresponding to 2-week foreshock and aftershock activity related with the M_L 5.0 events. The green curves indicate the positive flower structures.

Time-dependent variations in frictional behavior along chain are suggested by the irregular spatio-temporal pattern of M_W 6.0 historical events (Fig. 6). Those variations are further supported by the OBS data, since the same patch that ruptured twice (27 April, $M_L = 5.2$; 20 August, $M_L = 5.0$), demonstrated different foreshock activity. This is indicative of highly variable faulting, exhibiting temporal features in addition to spatial segmentation. Such temporal variations may be caused by the temporal changes in pore pressure due to fluid circulation, leading to subsequent draining and fluid saturation stages. They may also lead to periodic hydration and dehydration of peridotite. Both effects can switch the rupture mode between seismic and aseismic slip depending on whether a positive or a negative feedback loop is activated (e.g., Renard, 2021). 3-D rate/state friction models suggest that TF segments switch between seismic and aseismic slip over many earthquake cycles (Liu et al., 2012). Time-dependent features are also supported by analysis of exhumed ancient oceanic TF rock samples (Cox et al., 2021). Note that a characteristic property of ser-

pentine is that, depending upon the applied strain rate it may demonstrate both seismic (frictional decrease under fast loading velocities) and aseismic (frictional increase under slow loading velocities) behavior. Thus, both stable and unstable slip propagation is plausible in the presence of serpentinized rocks (Reinen et al., 1991).

Conclusions

We investigate the seismotectonic properties along Chain TF at the equatorial MAR by combining geophysical data with a ~1-year OBS seismicity data and 30-year historical earthquake data. OBS seismicity rates in a given area are not always directly related to the presence or absence of large historical earthquakes. However, the patches with the highest OBS seismicity rates have not hosted M_W 6.0 events. Our analysis reveals three OBS seismicity clusters which divide Chain into western, central and eastern areas. We find that OBS seismicity occurs at much higher rates at the eastern part of Chain (~300 events/°), co-located with the largest flower structure (transpressional morphological feature) and negative rMBA values. The majority of seismic moment is released at the western and central areas with much less moment release in the eastern area, as inferred from both OBS and historical data. There are two 50-75 km long segments (asperities) with moderate to low OBS seismicity rates (~100 events/°), occasionally hosting M_W 6.0 earthquakes. These 2 segments are separated by three 40 – 65 km long historical seismicity gaps, with few historical earthquakes with 5.5 $M_W < 6.0$, but generally high OBS seismicity (>200 events/°). There is no evidence of dynamic triggering from remote earthquakes and weak evidence of tidal triggering beneath ELFS. Potential static stress triggering is only detected in connection to the stronger OBS event (M_L = 5.4) along Chain. We find higher b-values in locations of lower rMBA and shallower bathymetry, likely indicative of thickened crust. The existence of seismic/aseismic patches, the differences between aseismic/seismic behavior in OBS vs. historical earthquakes, and the non-regular occurrence of large events implies heterogeneity along the fault, possibly due to variable hydrothermal circulation/alteration. These results also suggest that earthquake occurrence rates and size in a given location can be variable in time. These variations are likely dictated by variations between regions characterized by hydrothermal alteration (barriers) and normal gabbroic crust/unaltered mantle lithosphere (asperities).

Data Availability Statement

The seismic data are archived at the IRIS DMC, as 2016–2017 network XS https://doi.org/10.7914/SN/XS_2016 (Rychert et al., 2016). The earthquake catalog used in the study is available as a pre-print from Schlaphorst et al. (doi: 10.1002/essoar.10511147.1). The global seismicity data come from GCMT, www.globalcmt.org/, last accessed March 2022. The relocated data come from Shi et al. (2021), available at https://doi.org/10.5281/zenodo.4646438, last accessed June 2021). Figure 1 was generated using Generic Mapping Tools v.6.1.1 (www.soest.hawaii.edu/gmt, last ac-

cessed March 2022). The code for the Anderson-Darling test can be downloaded from https://git.plgrid.pl/projects/EA/repos/sera-applications/browse/, last accessed March 2022. CFF calculations are performed with the *Coulomb* software package available at https://www.usgs.gov/node/279387 (last accessed January, 2022). The stress inversion from focal mechanisms was performed with the *stressinverse* software package available at https://www.ig.cas.cz/stress-inverse/ (last accessed March, 2022)

Acknowledgements

K. Leptokaropoulos, C. A. Rychert and N. Harmon acknowledge funding from the Natural Environment Research Council (NE/M003507/1) and the European Research Council (GA 638665). J. -M. Kendall was funded by the Natural Environment Research Council (NE/M004643/1). We thank the captain and crew of the R/V Marcus G. Langseth and the RRS Discovery, and also the scientific technicians.

References

1. Abercrombie R. E., & Ekström G. (2001). Earthquake slip on oceanic transform faults. *Nature*, 410, 74-77

2. Aderhold, K., & Abercrombie R. E. (2016). The 2015 Mw 7.1 earthquake on the Charlie-Gibbs transform fault: Repeating earthquakes and multimodal slip on a slow oceanic transform. *Geophysical Research Letters*, 43, 6119–6128, doi:10.1002/2016GL068802

3. Agius, M. R., Harmon, N., Rychert, C. A., Tharimena, S., & Kendall J. M. (2018). Sediment characterization at the equatorial Mid-Atlantic Ridge from P-to-S teleseismic phase conversions recorded on the PI-LAB experiment. *Geophysical Research Letters*, 45, 12,244–12,252, doi: 10.1029/2018GL080565

4. Agius, M. R., Rychert, C. A., Harmon, N., Tharimena, S., & Kendall J. M. (2021). A thin mantle transition zone beneath the equatorial Mid-Atlantic Ridge. *Nature*, doi: 10.1038/s41586-020-03139-x

5. Agnew, D. C. (1997). NLOADF: A program for computing ocean-tide loading, *Journal of Geophysical Research.* 102, 5109–5110, doi.org/10.1029/96jb03458

6. Aki, K. (1965). Maximum likelihood estimate of b in the formula logN = a - bM and its confidence limits. *Bulletin of Earthquake Research Institute of the University of Tokyo*, 43, 237–239

7. Amorèse D, Grasso, J.-R., & Rydelek, P.A. (2010). On varying b values with depth: results from computer-intensive tests for Southern California. *Geophysical Journal International*, 180, 347–360, doi: 10.1111/j.1365-246X.2009.04414 .x

8. Behn, M. D., Boettcher, M. S., & Hirth, G. (2007). Thermal structure of oceanic transform faults. *Geology*, 35, 307-310, doi: 10.1130/G23112A.1

9. Blackman, D. K., Cann, J. R., Janssen, B., & Smith, D. K. (1998). Origin of extensional core complexes: evidence from the Mid-Atlanic Ridge at Atlantis Fracture Zone. *Journal of Geophysical Research: Solid Earth,* 103, 21315–21333

10. Boettcher, M. S., & Jordan, T. H. (2004). Earthquake scaling relations for mid-ocean ridge transform faults. *Journal of Geophysical Research*, 109, B12302, doi: 10.1029/2004JB003110

11. Boettcher, M. S., & McGuire, J. J. (2009). Scaling relations for seismic cycles on mid-ocean ridge transform faults. *Geophysical Research Letters*, doi:10.1029/2009GL040115

12. Bogiatzis, P., Karamitrou, A., Ward Neale, J., Harmon, N., Rychert, C. A., & Srokosz, M. (2020). Source regions of infragravity waves recorded at the bottom of the equatorial Atlantic Ocean, using OBS of the PI-LAB experiment. *Journal of Geophysical Research: Oceans*, 125, e2019JC015430, https://doi.org/10.1029/2019JC015430

13. Brune, J. N. (1968). Seismic moment, seismicity, and rate of slip along major fault zones. *Journal of Geophysical Research*, 73, 777–784

14. Cann, J. R., Blackman, D. K., Smith, D. K., McAllister, E., Janssen, B., Mello, S., et al. (1997). Corrugated slip surfaces formed at ridge-transform intersections on the Mid-Atlantic Ridge. *Nature,* 385, 329–332, doi: 10.1038/385329a0

15. Cox, S., Fagereng, A., & MacLeod, C. J. (2021). Shear zone development in serpentinized mantle: Implications for the strength of oceanic transform faults. *Journal of Geophysical Research: Solid Earth,* 126, e2020JB020763

16. Deng, J., & Sykes, L. R. (1997). Stress evolution in southern California and triggering of moderate, small, and micro-size earthquakes. *Journal of Geophysical Research*, 102, 24,411-24,435

17. Dymkova, D., & Gerya, T. (2013). Porous fluid flow enables oceanic subduction initiation on Earth. *Geophysical Research Letters*, 40, 5671–5676

18. Ekström, G., Nettles, M., & Dziewoński, A. (2012). The global CMT project 2004–2010: centroid-moment tensors for 13,017 earthquakes. *Physics of the Earth and Planetary Interiors*, 200–201, 1–9 (2012)

19. Egbert, G. D., & Erofeeva, S. Y. (2002). Efficient inverse modeling of barotropic ocean tides. *Journal of Atmospheric and Oceanic Technology*, 19, 183–204. https://doi.org/10.1175/1520-0426(2002)019<0183:eimobo>2.0.co;2

20. Engeln, J. F., Wiens, D. A., & Stein, S. (1986). Mechanisms and depths of Atlantic transform earthquakes. *Journal of Geophysical Research*, 91, 548–577

21. Escartín, J., Hirth, G., & Evans, B. (1997). Nondilatant brittle deformation of serpentinites: Implications for Mohr-Coulomb theory and the strength of faults. *Journal of Geophysical Research*, 102, 2897-2913

22. Escartín, J., & Cannat, M. (1999). Ultramafic exposures and gravity signature of the lithosphere near the Fifteen-Twenty Fracture Zone (Mid-Altlantic Ridge, 14o-16.5oN). *Earth and Planetary Science Letters*, 171, 411–424. doi: 10.1016/S0012-821X(99) 00169-7

23. Escartín, J., Hirth, G., & Evans, B. (2001). Strength of slightly serpentinized peridotites: implications for the tectonics of oceanic lithosphere. *Geology*, 29, 1023–1026

24. Fojtíková, L., & Vavryčuk, V. (2018). Tectonic stress regime in the 2003-2004 and 2012-2015 earthquake swarms in the Ubaye Valley, French Alps. *Pure and Applied Geophysics*, 175, 1997-2008

25. Früh-Green, G. L., Orcutt, B. N., Green, S. L., & Cotterill, C. (2016). *Atlantis massif serpentinization and life,* in Proceedings of the International Ocean Discovery Program, (College Station, TX: International Ocean Discovery Program), 357, doi: 10.14379/iodp.proc.357.2017

26. Froment, B., McGuire, J. J., van der Hilst, R. D., Gouedard, P., Roland, E. C., Zhang, H., & Collins, J. A. (2014). Imaging along-strike variations in mechanical properties of the Gofar transform fault, East Pacific Rise. *J. Geophys. Res. Solid Earth* 119, 7175–7194

27. Gomberg, J., Bodin, P., Larson, K., & Dragert, H. (2004). Earthquakes nucleated by transient deformations caused by the M = 7.9 Denali, Alaska, earthquake, *Nature,* 427, 621–624

28. Gregg, P. M., Lin, J., Behn, M. D., & Montési, L. G. J. (2007). Spreading rate dependence of gravity anomalies along oceanic transform faults, *Nature*, 448, doi:10.1038/nature05962

29. Gregory, E. P. M., Singh, S. C., Marjanović, M., & Wang, Z. (2021). Serpentinized peridotite versus thick mafic crust at the Romanche oceanic transform fault. *Geology*, v. 49, p. 1132–1136, https://doi.org/10.1130/G49097.1

30. Grevemeyer, I., Reston T. J., & Moeller, S. (2013). Microseismicity of the Mid-Atlantic Ridge at 7°S–8°15'S and at the Logatchev Massif oceanic core complex at 14°40'N–14°50'N. *Geochemistry Geophysics Geosystems*, 14, 3532-3554, doi: 10.1002/ggge.20197

31. Hallo, M., Opršal, I., Asano, K., & Gallovič, F. (2019). Seismotectonics of the 2018 northern Osaka M6.1 earthquake and its aftershocks: joint

movements on strike-slip and reverse faults in inland Japan. *Earth Planets Space*, 71:34

32. Hanks, T. C., & Kanamori, H. (1979). A moment magnitude scale. *Journal of Geophysical Research*, 84 (B5), 2348–50

33. Harmon, N., Rychert, C. A., Agius, M., Tharimena, S., Le Bas, T., Kendall, J. M., & Constable, S. (2018). Marine geophysical investigation of the Chain Fracture Zone in the equatorial Atlantic from the PI-LAB experiment. *Journal of Geophysical Research: Solid Earth*, 123, 11,016–11,030, https://doi.org/10.1029/ 2018JB015982

34. Harmon, N., Rychert, C. A., Kendall, J. M., Agius, M., Bogiatzis, P., & Tharimena, S. (2020). Evolution of the oceanic lithosphere in the equatorial Atlantic from Rayleigh wave tomography, evidence for small-scale convection from the PI-LAB experiment. *Geochemistry Geophysics Geosystems*, 21, e2020GC009174, doi: 10.1029/2020GC009174

35. Harmon, N., Wang, S., Rychert, C. A., Constable, S., & Kendall, J. M. (2021). Shear velocity inversion guided by resistivity structure from the PI-LAB experiment for integrated estimates of partial melt in the mantle. *Journal of Geophysical Research: Solid Earth*, 126, e2021JB022202. https://doi. org/10.1029/2021JB022202

36. Harris, R. A. (1998). Introduction to special section: Stress triggers, stress shadows and implications for seismic hazard. *Journal of Geophysical Research*, 103, 24,347-24,358

37. Hensen C., Duarte J. C., Vannucchi P., Mazzini A., Lever M. A., Terrinha P., Géli L., et al. (2019). Marine Transform Faults and Fracture Zones: A Joint Perspective Integrating Seismicity, Fluid Flow and Life, *Frontiers in Earth Science*, 7:39. doi: 10.3389/feart.2019.00039

38. Hicks, S.P., Okuwaki, R., Steinberg, A., Rychert, C. A., Harmon, N., Abercrombie, R., Bogiatzis, P., et al. (2020). Back-propagating supershear rupture in the 2016 Mw 7.1 Romanche transform fault earthquake. *Nature Geoscience*, 13, 647–653, doi: 10.1038/s41561-020-0619-9

39. Karato, S.-I., Paterson, M., & Fitzgerald, D. (1986). Rheology of synthetic olivine aggregates: Influence of grain size and water. *Journal of Geophysical Research*, 91, 8151–8176

40. Kelley, D. S., Karson, J. A., Blackman, D. K., Früh-Green, G. L., Butterfield, D. A., Lilley, M. D., et al. (2001). An off-axis hydrothermal vent field near the Mid-Atlantic Ridge at 30°N. *Science*, 412, 145–149

41. Kohli, A., Wolfson-Schwehr, M., Prigent, C., & Warren, J. M. (2021). Oceanic transform fault seismicity and slip mode influenced by seawater infiltration. *Nature Geoscience*, 14, 606-611

42. Kuna, V. M., Nabělek J. L., & Braunmiller, J. (2019). Mode of slip and crust–mantle interaction at oceanic transform faults, *Nature Geoscience*, 12, 138–142

43. Lasocki S. (2014). Transformation to equivalent dimension - a new methodology to study earthquake clustering. *Geophysical Journal International*, 197, 1224-1235, doi:10.1093/gji/ggu062

44. Leptokaropoulos K., Karakostas, V., Papadimitriou, E., Adamaki, A., Tan, O., & İnan, S. (2013). A Homogeneous Earthquake for Western Turkey and Magnitude of Completeness Determination. *Bulletin of the Seismological Society of America*, 103, 5, 2739-2751, doi: 10.1785/0120120174

45. Leptokaropoulos, K. (2020). Magnitude distribution complexity and variation at The Geysers geothermal field. *Geophysical Journal International, 222*, 893-906, doi: 10.1093/gji/ggaa208

46. Leptokaropoulos, K., Harmon, N., Hicks, S., Rychert, C. A., Schlaphorst, D., & Kendall, J. M. (2021). Tidal Triggering of Microseismicity at the Equatorial Mid-Atlantic Ridge, Inferred from the PI-LAB experiment. *Journal of Geophysical Research: Solid Earth*, 126, e2021JB022251, doi: 10.1029/2021JB022251

47. Lin, J., & Stein, R. S. (2004). Stress triggering in thrust and subduction earthquakes, and stress interaction between the southern San Andreas and nearby thrust and strike-slip faults. *Journal of Geophysical Research*, v. 109, B02303, doi:10.1029/2003JB002607

48. Linker, J., & Dieterich J. (1992). Effects of variable normal stress on rock friction: observations and constitutive equations. *Journal of Geophysical Research*, 97, 4923–4940, doi:10.1029/92JB00017

49. Liu, Y., McGuire, J. J., & Behn, M. D. (2012). Frictional behavior of oceanic transform faults and its influence on earthquake characteristics. *Journal of Geophysical Research*, 117, B04315

50. Marsaglia, G., & Marsaglia, J. (2004). Evaluating the Anderson-Darling distribution. *Journal of Statistical Software*, 9, 1-5

51. Marjanović, M., Singh, S. C., Gregory, E. P. M., Grevemeyer, I., Growe, K., Wang, Z., et al. (2020). Seismic crustal structure and morphotectonic features associated with the Chain Fracture Zone and their role in the evolution of the equatorial Atlantic region. *Journal of Geophysical Research: Solid Earth*, 125, e2020JB020275, doi: 10.1029/2020JB020275

52. McGuire, J. J., Collins, J. A., Gouedard, P., Roland, E., Lizarralde, D., Boettcher, M. S., Behn, M. D., & van der Hilst, R. D. (2012). Variations in earthquake rupture properties along the Gofar transform fault, East Pacific Rise. *Nature Geoscience,* 5, 336–341

53. Meredith, P. G., & Atkinson, B. K. (1985). Fracture toughness and subcritical crack grown during high temperature tensile deformation of westerly granite and black gabbro. *Physics of the Earth and Planetary Interiors*, 39(1): 33–51, doi: 10.1016/0031–9201(85)90113-x

54. Molnar, P. (2020). The brittle-plastic transition, earthquakes, temperatures, and strain rates. *Journal of Geophysical Research: Solid Earth*, 125, e2019JB019335. doi: /10.1029/2019JB019335

55. Moore, D. E., Lockner, D. A., Ma, S. L., Summers, R., & Byerlee, J. D. (1997). Strengths of serpentinite gouges at elevated temperatures. *Journal of Geophysical Research: Solid Earth*, 102, 14787–14801

56. Olive, J.-A., & Escartín, J. (2016). Dependence of seismic coupling on normal fault style along the Northern Mid-Atlantic Ridge. *Geochemistry Geophysics Geosystems*, 17, 4128–4152, doi:10.1002/ 2016GC006460.

57. Pan, J., Antolik, M., & Dziewonski, A. M. (2002). Locations of mid-oceanic earthquakes constrained by seafloor bathymetry. *Journal of Geophysical Research*, 107, B11, 2310, doi: doi:10.1029/2001JB001588

58. Parsons, T., Stein, R. S., Simpson, R. W., & Reasenberg, P. A. (1999), Stress sensitivity of fault seismicity; a comparison between limited-offset oblique and major strike-slip faults. *Journal of Geophysical Research*, v. 104, p. 20183-20202.

59. Reinen, L. A., Weeks, J. D., & Tullis, T. E. (1991). The frictional behavior of serpentinite: Implications for aseismic creep. *Geophysical Research Letters*, 18, 1921–1924, doi:10.1029/91GL02367

60. Renard, F. (2021). Reaction-induced fracturing: when chemistry breaks rocks. *Journal of Geophysical Research: Solid Earth*, 126, e2020JB021451

61. Roland, E., Behn, M. D., & Hirth, G. (2010). Thermal-mechanical behavior of oceanic transform faults: Implications for the spatial distribution of seismicity. *Geochemistry Geophysics Geosystems*, 11, Q07001, doi: 10.1029/2010GC003034

62. Roland, E., Lizarralde, D., McGuire, J. J., & Collins, J. A. (2012). Seismic velocity constraints on the material properties that control earthquake behavior at the Quebrada-Discovery-Gofar transform faults, East Pacific Rise. *Journal of Geophysical Research: Solid Earth,* 117, doi: 10.1029/2012jb009422

63. Rychert, C., Kendall, J. M., & Harmon, N. (2016). *Passive imaging of the lithosphere-asthenosphere boundary [data set].* International Federation of Digital Seismograph Networks. https://doi.org/10.7914/SN/XS_2016

64. Rychert, C. A., Tharimena, S., Harmon, N., Wang, S., Constable, S., Kendall, J. M., Bogiatzis, P., Agius, M. G., & Schlaphorst, D. (2021).

A dynamic lithosphere–asthenosphere boundary near the equatorial Mid-Atlantic Ridge. *Earth and Planetary Science Letters*, 566, 116949, doi: 10.1016/j.epsl.2021.116949

65. Saikia, U., Rychert, C., Harmon, N., & Kendall, J. M. (2020). Sediment structure at the equatorial mid-atlantic ridge constrained by seafloor admittance using data from the PI-LAB experiment. *Marine Geophysical Research*, 41, 3, doi: 10.1007/s11001-020-09402-0

66. Saikia, U., Rychert, C., Harmon, N., & Kendall, J. M. (2021a). Upper mantle anisotropic shear velocity structure at the equatorial Mid-Atlantic ridge constrained by Rayleigh wave group velocity analysis from the PI-LAB experiment. *Geochemistry Geophysics Geosystems,* **22**, e2020GC009495, (2021a)

67. Saikia, U., Rychert, C., Harmon, N., & Kendall, J. M. (2021b). Seismic attenuation at the equatorial Mid-Atlantic Ridge constrained by local Rayleigh wave analysis from the PI-LAB experiment. *Geochemistry Geophysics Geosystems*, **22**, e2021GC010085. (2021b)

68. Schlaphorst, D., Rychert, C., Harmon, N., Hicks, S., Bogiatzis, P., Kendall, J. M., & Abercrombie, R. (2022). Local seismicity around the Chain Transform Fault at the Mid-Atlantic Ridge from OBS observations. *Preprint submitted in Geophysical Journal International, doi: 10.1002/essoar.10511147.1*

69. Scholz, C. (2019). *The Mechanics of Earthquakes and Faulting* (3rd ed.). Cambridge: Cambridge University Press. doi:10.1017/9781316681473

70. Schuster, A. (1897). On lunar and solar periodicities of earthquakes. *Proceedings of the Royal Society of London*, 61, 455–465. https://doi.org/10.1098/rspl.1897.0060

71. Shi, P., Meng, W., & Pockalny, R. (2021). The ubiquitous creeping segments on oceanic transform faults. *Geology*, XX, X, doi.org/10.1130/G49562.1

72. Siegel, A. F. (1982). Robust regression using repeated medians. *Biometrika*, 69, 242–244

73. Silverman, B.W. (1986). *Density Estimation for Statistics and Data Analysis*, Monograph, CRC Press, 175 pp

74. Simão, N., Escartín, J., Goslin, J., Haxel, J., Cannat, M., & Dziak, R. (2010). Regional seismicity of the Mid-Atlantic Ridge: observations from autonomous hydrophone arrays, *Geophysical Journal International*, 183, 1559-1578, doi: 10.1111/j.1365-246X.2010.04815.x

75. Stein, R. S. (1999). The role of stress transfer in earthquake occurrence. *Nature*, 402, 605 – 609

76. Toda, S., Stein, R. S., Richards-Dinger, K., & Bozkurt, S. (2005). Forecasting the evolution of seismicity in southern California: Animations built on earthquake stress transfer. *Journal of Geophysical Research*, v. 110, B05S16, doi:10.1029/2004JB003415

77. Vavryčuk, V. (2014). Iterative joint inversion for stress and fault orientations from focal mechanisms. *Geophysical Journal International*, 199, 69-77, doi: 10.1093/gji/ggu224

78. Wang, S., Constable, S., Rychert, C. A., & Harmon, N. (2020). A Lithosphere-Asthenosphere Boundary and Partial Melt Estimated Using Marine Magnetotelluric Data at the Central Middle Atlantic Ridge. *Geochemistry Geophysics Geosystems*, 21, e2020GC009177, doi: 10.1029/2020GC009177

79. Ward, J. H., (1963). Hierarchical grouping to optimize an objective function. *Journal of the American Statistical Association*, 58, 236–244

80. Wells, D. L., & Coppersmith, K. J. (1994). New empirical relationships among magnitude, rupture length, rupture width, rupture area, and surface displacement. *Bulletin of the Seismological Society of America*, 84, 974–1002

81. Wiemer, S., & Wyss, M. (2000). Minimum magnitude of completeness in earthquake catalogs: Examples from Alaska, the Western United States, and Japan. *Bulletin of the Seismological Society of America*, 90 (4), 859–869

82. Wilcock, W. S. D. (2009). Tidal triggering of earthquakes in the Northeast Pacific Ocean. *Geophysical Journal International*, 179, 1055-1070, doi: 10.1111/j.1365-246X.2009.04319.x

83. Wolfson-Schwehr, M., Boettcher, M. S., McGuire, J. J., & Collins, J. A. (2014). The relationship between seismicity and fault structure on the Discovery transform fault, East Pacific Rise. *Geochemistry Geophysics Geosystems*, 15, 3698–3712, doi:10.1002/2014GC005445

84. Wolfson-Schwehr, M., & Boettcher, M. S. (2019). *"Chapter 2 – global characteristics of oceanic transform fault structure and seismicity". In Transform Plate Boundaries and Fracture Zones*, ed. J. C. Duarte (Amsterdam: Elsevier). 21–59. doi: 10.1016/B978-0-12-812064-4.00002-5